Article

Synthesis of Magnetic α-Fe$_2$O$_3$/Rutile TiO$_2$ Hollow Spheres for Visible-Light Photocatalytic Activity

Zhongli Zhou [1], Hang Yin [1], Yuling Zhao [1,2], Jianmin Zhang [3,4], Yahui Li [1], Jinshi Yuan [1], Jie Tang [5,*] and Fengyun Wang [1,2,*]

[1] College of Physics, Qingdao University, No. 308 Ningxia Road, Qingdao 266071, China; zhouzl1019@163.com (Z.Z.); hangyinccc@gmail.com (H.Y.); zhaoyuling@qdu.edu.cn (Y.Z.); lyh_kitou@163.com (Y.L.); yuanjinshi@foxmail.com (J.Y.)

[2] State Key Laboratory of Bio Fibers and Eco Textiles, Qingdao University, No. 308 Ningxia Road, Qingdao 266071, China

[3] National Engineering Research Center for Intelligent Electrical Vehicle Power System, Qingdao University, No. 308 Ningxia Road, Qingdao 266071, China; jamiede@163.com

[4] School of Mechanical and Electrical Engineering, Qingdao University, No. 308 Ningxia Road, Qingdao 266071, China

[5] National Institute for Materials Science, 1-2-1 Sengen, Tsukuba 3050047, Japan

[*] Correspondence: tang.jie@nims.go.jp (J.T.); fywang@qdu.edu.cn (F.W.)

Abstract: The high recombination rate of the electron-hole pair on the surface of rutile TiO$_2$ (RT) reduces its photocatalytic performance, although it has high thermodynamic stability and few internal grain defects. Therefore, it is necessary for RT to develop effective methods to reduce electron-hole pair recombination. In this study, magnetic α-Fe$_2$O$_3$/Rutile TiO$_2$ self-assembled hollow spheres were fabricated via a facile hydrothermal reaction and template-free method. Based on the experimental result, phosphate concentration was found to play a crucial role in controlling the shape of these hollow α-Fe$_2$O$_3$/RT nanospheres, and the optimal concentration is 0.025 mM. Due to a heterojunction between α-Fe$_2$O$_3$ and RT, the electron-hole pair recombination rate was reduced, the as-synthesized hollow α-Fe$_2$O$_3$/RT nanospheres exhibited excellent photocatalysis in rhodamine B (RhB) photodegradation compared to α-Fe$_2$O$_3$ and RT under visible-light irradiation, and the degradation rate was about 16% (RT), 60% (α-Fe$_2$O$_3$), and 93% (α-Fe$_2$O$_3$/RT) after 100 min. Moreover, α-Fe$_2$O$_3$/RT showed paramagnetism and can be recycled to avoid secondary environmental pollution.

Keywords: α-Fe$_2$O$_3$; rutile TiO$_2$; template-free method; phosphate; heterojunction; photocatalytic activity; rhodamine B

1. Introduction

Semiconductor photocatalysis is an advanced environmental purification technology that converts solar energy into chemical energy [1–4]. This promising technology can oxidize organic pollutants through superoxide anions or hydroxyl radicals produced by photo-electrons or photo-generated holes [5,6]. Titanium dioxide (TiO$_2$), as a typical photocatalytic material, has excellent photocatalytic properties. Many studies have shown that the photocatalytic activity of anatase crystal TiO$_2$ is much greater than that of rutile crystal, and it has received extensive attention and applications [7,8]. Theoretically, compared with the anatase crystal form, the rutile crystal form TiO$_2$ has higher thermodynamic stability and fewer internal grain defects. However, it does not show comparable photocatalytic performance. One of the main reasons is that rutile TiO$_2$ has a high carrier recombination rate, limiting its photocatalytic activity. Therefore, how to improve the separation efficiency of photogenerated carriers of rutile TiO$_2$ is an urgent problem to be solved [9–11].

Compared with anatase TiO$_2$ (AT), RT has a relatively narrow bandgap and can absorb more solar energy than AT in the near-ultraviolet region (wavelength: 360–400 nm) [12]. However, since electron-hole pairs are easy to recombine, the photocatalytic performance

is affected. To address this issue, researchers have done a lot of work. For example, the enhancement of photocatalytic performance of TiO_2 by using various strategies such as doping, semiconducting heterojunction, heterostructure [13], and anatase-rutile combination has been successful. Xu et al. [14] synthesized rutile/anatase TiO_2 heterojunction nanoflowers via a facile one-step hydrothermal approach, which showed excellent stability. Researchers introduced low band gap materials with TiO_2 heterojunctions, designed nanomorphologies to improve the charge separation, increase active sites, etc., in their work. Ghosh et al. [15] reported a set of mesoporous, hierarchical "nanorods-on-nanofiber" heterostructures produced from the organization of V_2O_5 nanorods on TiO_2 nanofibers fabricated using a gas jet fiber spinning process. Zhang et al. [16] fabricated a novel three-dimensional Fe_2O_3 nanorod/TiO_2 nanosheet heterostructure via the facile hydrothermal and chemical bath deposition methods and this structure exhibited the superior photocatalytic. Semiconductor hematite (α-Fe_2O_3), with a bandgap between 1.9 and 2.2 eV, is usually thermodynamically stable and can be used as a photocatalyst to decompose water and degrade organic pollutants [17]. α-Fe_2O_3 has strong visible light absorption, stability, and other advantages, such as magnetism, recyclability, and no secondary pollution for the environment. However, due to its low carrier mobility and the short excited-state lifetime, α-Fe_2O_3 usually exhibits weaker photocatalytic performance [18]. Therefore, we combined RT with visible light-responsive α-Fe_2O_3 to form a heterojunction. The excitable electrons on the α-Fe_2O_3 conduction band (CB) can be transferred to the RT' valence band (VB) across the barrier, which can improve the electron transfer ability of α-Fe_2O_3 and extend the lifetime of excited electrons. The holes on the RT are transferred to α-Fe_2O_3, making up for the deficiency of the high recombination rate of RT electron holes, enhancing charge separation, and improving photocatalytic performance.

Luan et al. [9] synthesized RT nanorod-coupled α-Fe_2O_3 by a wet-chemical process, which confirmed that the coupling of an appropriate amount of RT nanorods with α-Fe_2O_3 could significantly enhance the feasibility of photoelectron chemical oxidation and degradation of pollutants. The researchers also confirmed that RT combined with visible light-responsive Fe_2O_3 can effectively increase the light absorption range and improve photocatalytic activity. Wang et al. [19] synthesized the mesoporous Fe_2O_3/TiO_2 heterostructure microspheres by the solvothermal method and optimized the preparation conditions. Liu et al. [20] prepared 3D α-Fe_2O_3@TiO_2 core-shell nanocrystals with three forms—rhombic, cubic, and disc-shaped—through hydrothermal and annealing processes. Xie et al. [21] developed a feasible route to enhance the visible photocatalytic activities of α-Fe_2O_3 nanoparticles for degrading colorless pollutants by coupling a proper amount of mesoporous nanocrystalline AT. Most researchers take α-Fe_2O_3 as the magnetic core and load TiO_2 onto its surface to form a core-shell structure. However, this structure may affect the magnetism of α-Fe_2O_3 because of the excessively thick TiO_2 loading, and it is difficult for α-Fe_2O_3 and TiO_2 to have a synergistic effect and improve the photocatalytic performance. The spherical hollow structure has been widely studied because of its advantages, such as high specific surface area, low density, high load-bearing capacity, and high refractive index [22–26].

Herein, we first synthesized an RT and α-Fe_2O_3 composite with a spherical hollow structure via a one-pot hydrothermal method without the template. The self-assembled hollow structures have a heterojunction structure that can effectively improve the photocatalytic activity. The morphology of the assembled structure is controlled by adjusting the amount of phosphate ion and proposes a possible reaction mechanism. We also explored the growth mechanism of hollow self-assembled composite structures through time-variable experiments. The obtained magnetic hollow self-assembled composite structure has enhanced photocatalytic activity, can be mass-produced, and can be recycled. Our synthetic method makes RT have potential application value in the field of photocatalytic degradation of organic pollutants.

2. Results and Discussion

2.1. Characterization

The XRD patterns (Figure 1) show the purity and crystallinity of the synthesized sample. Several peaks were observed in the positions of 24.13°, 33.15°, 35.61°, 40.85°, 49.17°, 54.08°, 62.44°, and 63.98° in the XRD patterns of α-Fe_2O_3/RT samples, which were indexed to the (0 1 2), (1 0 4), (1 1 0), (1 1 3), (0 2 4), (1 1 6), (2 1 4), and (3 0 0) crystal planes of α-Fe_2O_3 (PDF 87-1165) [16]. Regarding the peak of RT, 27.44° corresponded to the (1 1 0), (1 0 1), (1 1 1), (2 1 1), and (3 1 0) crystal planes of RT (PDF 76-1941) [14]. According to the full width at half-maximum (fwhm) of the diffraction peaks, the average crystallite size of the α-Fe_2O_3 crystallites (phosphate addition of 0 mM, 0.025 mM, and 0.042 mM) could be estimated from the Scherrer equation to be about 420.3, 375.4, and 401.2 nm, respectively; the average crystallite size of the RT crystallites (phosphate addition of 0 mM, 0.025 mM, and 0.042 mM) could be estimated from the Scherrer equation to be about 468.5, 450.3, and 474.2 nm, respectively.

$$D_{hkl} = K\lambda/(\beta_{hkl} \cos \theta_{hkl})$$

where D_{hkl} is the particle size perpendicular to the normal line of the (*hkl*) plane, *K* is a constant (0.89), β_{hkl} is the full width at half-maximum of the (*hkl*) diffraction peak, θ_{hkl} is the Bragg angle of (*hkl*) peak, and λ is the wavelength of the X-ray. No other peaks were observed, demonstrating that the α-Fe_2O_3 and RT had high purity and high crystallinity, which are advantageous for enhancing the photocatalytic activity under visible light irradiation.
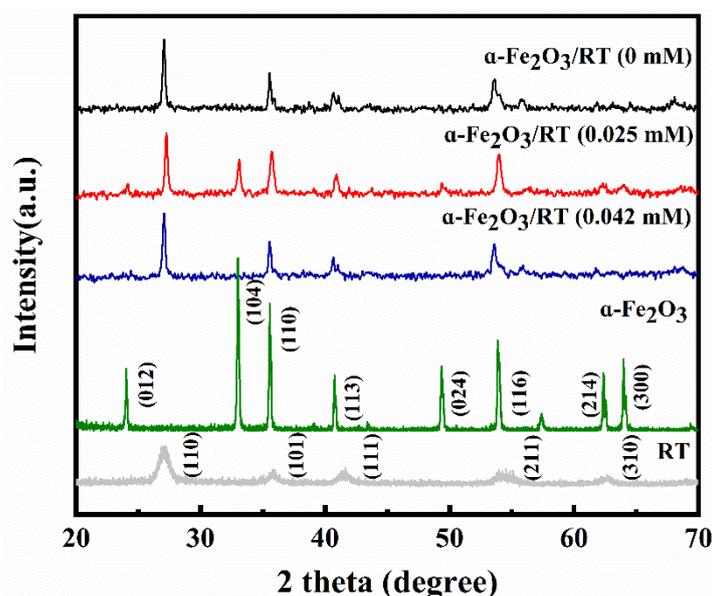

Figure 1. XRD patterns of α-Fe_2O_3/RT with phosphate addition of 0 mM, 0.025 mM, and 0.042 mM; α-Fe_2O_3 and RT.

The morphology of pure RT and α-Fe_2O_3 is shown in Figure 2. The agglomeration of all particles was severe. Sufficient active sites could not be exposed, which was not conducive to photocatalytic reactions and reduced photocatalytic activity. In addition, RT (Figure 2a) had a spherical structure with an average particle size of 17 nm according to the histogram of the particle size distribution (Figure 2b), and α-Fe_2O_3 (Figure 2c) was an ellipse with an average particle size of 1.1 μm (Figure 2d). Figure 3a–c are the SEM images of α-Fe_2O_3/RT (0 mM) with many agglomerated particles. When the phosphate concentration was up to 0.025 mM (Figure 3d–f), hollow α-Fe_2O_3/RT nanospheres were formed and assembled by pyramid-shaped particles. As shown in Figure 3e, some broken α-Fe_2O_3/RT microspheres revealed that the as-obtained α-Fe_2O_3/RT nanospheres were of the hollow structure. Figure 3g–i SEM images of α-Fe_2O_3/RT (0.042 mM) show that

the sample's shell became thicker than the addition of 0.025mM α-Fe$_2$O$_3$/RT, and the morphology of the assembled unit became irregular.
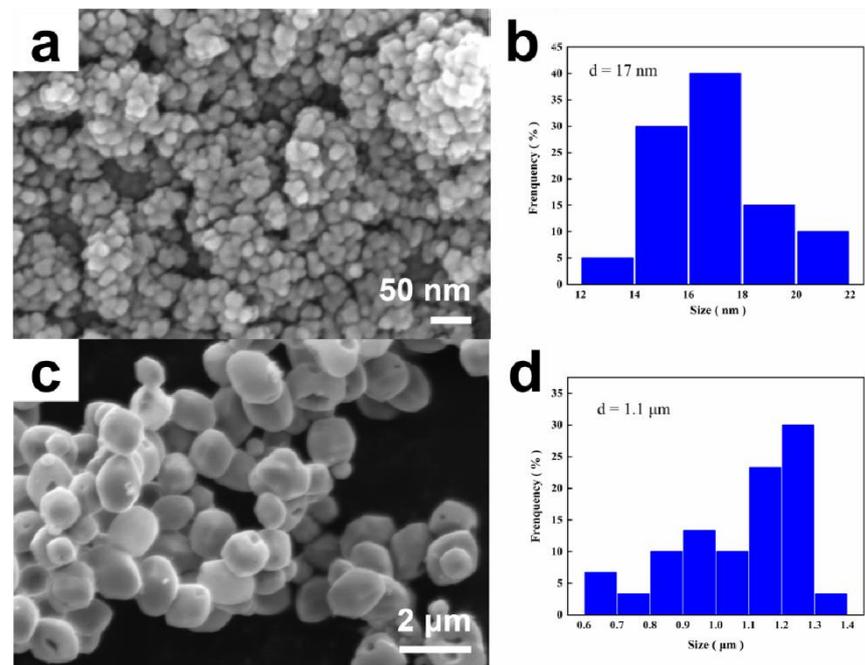

Figure 2. (**a**) SEM of RT and (**b**) histogram of the particle size distribution; (**c**) SEM of α-Fe$_2$O$_3$ and (**d**) histogram of the particle size distribution.
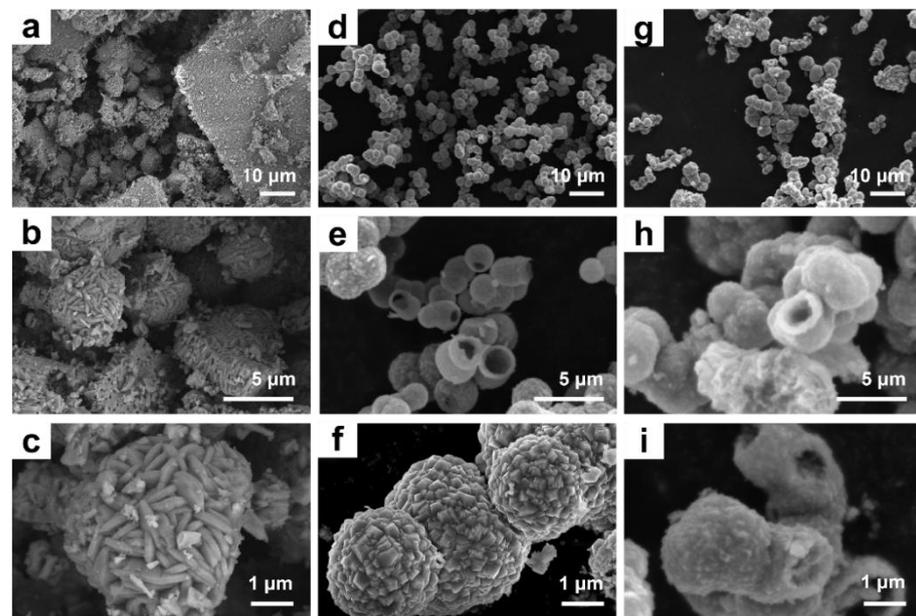

Figure 3. SEM of α-Fe$_2$O$_3$/RT prepared with varying additions of phosphate: (**a–c**) 0 mM, (**d–f**) 0.025 mM, and (**g–i**) 0.042 mM.

To further understand the composition of α-Fe$_2$O$_3$/RT, we performed an EDX analysis, as shown in Figure 4. Fe, Ti, and O were evenly distributed on the sphere. Figure 5a–c are the typical TEM images of α-Fe$_2$O$_3$/RT (phosphate addition was 0.025 mM) nanospheres (about 1.5 µm) with hollow structures assembled by nanoparticles. Furthermore, the intimate heterojunctions between α-Fe$_2$O$_3$ and RT were formed utilizing the High Resolution Transmission Electron Microscope (HRTEM) image (Figure 5d). The facet distances of

0.32 nm and 0.25 nm corresponded to the α-Fe_2O_3 (1 1 0) [9] crystal plane and RT (1 1 0) [27] crystal plane, respectively. The clear stripes show that the composite material had good crystallinity. This heterojunction structure was conducive to electron transfer.
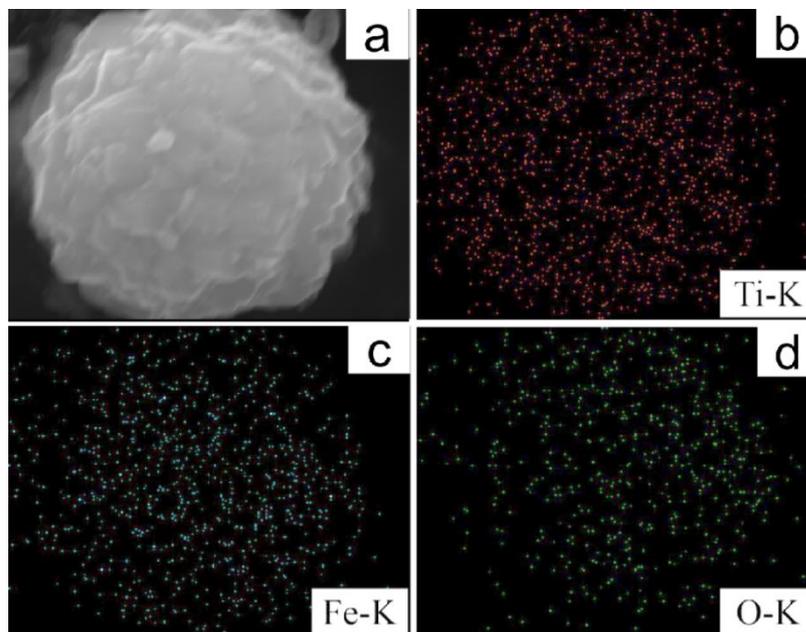

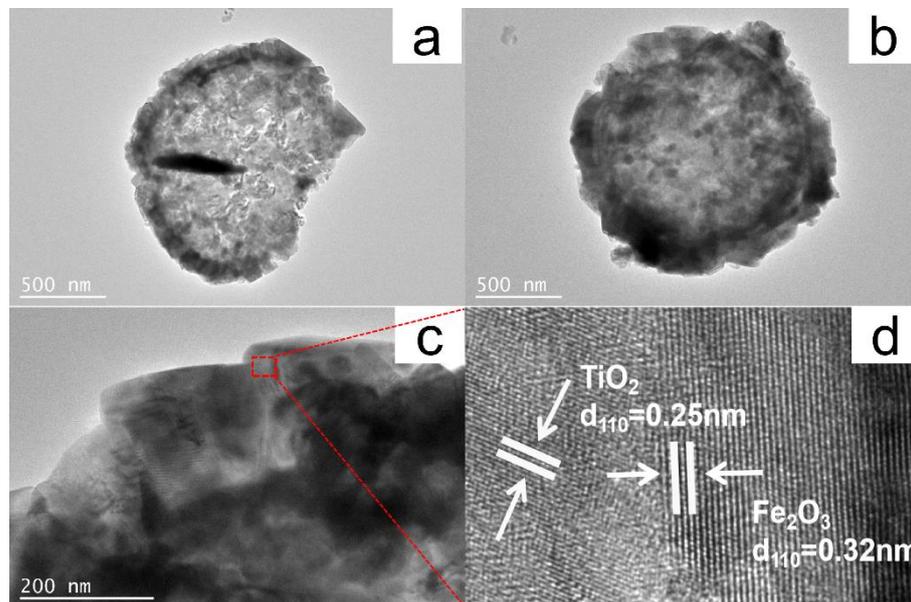**Figure 4.** (**a–d**) Ti, Fe, and O elemental mapping.

Figure 5. (**a–c**) Low and high magnification TEM images and (**d**) HRTEM image of α-Fe_2O_3/RT (0.025 mM).

As expected, the composite hollow structure's morphology could be controlled by adjusting the concentration of phosphate ions ($H_2PO_4^-$). The introduction of $H_2PO_4^-$ reduces the pH of the reaction system. A low pH can suppress the dissolution of the intermediate product α-FeOOH substrate [28–31]. Since the slow dissolution of an α-FeOOH substrate promotes α-Fe_2O_3 nucleation, the addition of $H_2PO_4^-$ anions may promote the directional aggregation growth process of α-Fe_2O_3 nuclei. In short, $H_2PO_4^-$ plays an essential role in the formation of the hollow sphere α-Fe_2O_3/RT, and a complete spheri-

cal structure cannot synthesize without $H_2PO_4^-$ due to the nucleation of α-Fe_2O_3 being inhibited. However, when $H_2PO_4^-$ is excessive, $H_2PO_4^-$ can decrease the concentration of α-Fe_2O_3 in the solution by promoting Equation (1) towards the right [32]. Therefore, much damage occurred to the spherical structure. Therefore, $H_2PO_4^-$ affected the sample particles' structure, which further affected the photocatalytic performance of α-Fe_2O_3/RT.

$$Fe_2O_3 + 2xH_2PO_4 + 6H^+ \rightleftharpoons 2[Fe(H_2PO_4)_x]^{3-x} + 3H_2O \tag{1}$$

To better understand the formation process of hollow α-Fe_2O_3/RT microspheres, time-dependent experiments were carried out. As shown in Figure 6, representative SEM images at different time intervals are displayed. When the reaction time was 3 h, the complete regular spherical particles were formed (Figure 6a), and the peaks of α-Fe_2O_3 and RT could be observed (Figure 6e). The crystallinity of the composite material was the best at 48h. When the reaction time was 16 h, the sample did not change too much, only pyramidal particles of different sizes appeared on the surface, and it was not evident (Figure 6b). However, when the reaction time reached 24 h (Figure 6c) and 48 h (Figure 6d), the spherical hollow sample appeared. The surface of the sample was covered with particles of different sizes. In response to the above experimental results, we proposed the growth mechanism and reaction principle of RT and α-Fe_2O_3, as shown in Figure 6f. In the beginning, the raw material forms a solid ball under high temperature and pressure. The formed α-Fe_2O_3/RT nanoparticles are unstable and tend to form hollow structures, which may be due to the minimization of interfacial energy [33]. As the reaction time is prolongs, a hollow structure is found in the center of the solid ball. The hollow structure expands and finally stops on the sphere's surface, forming a spherical shell, and the surface is loaded with α-Fe_2O_3 and RT [34–36]. The hollow structure's formation is that small particles gradually adhere to large particles to form a sheet, commonly known as the Ostwald ripening process [37].
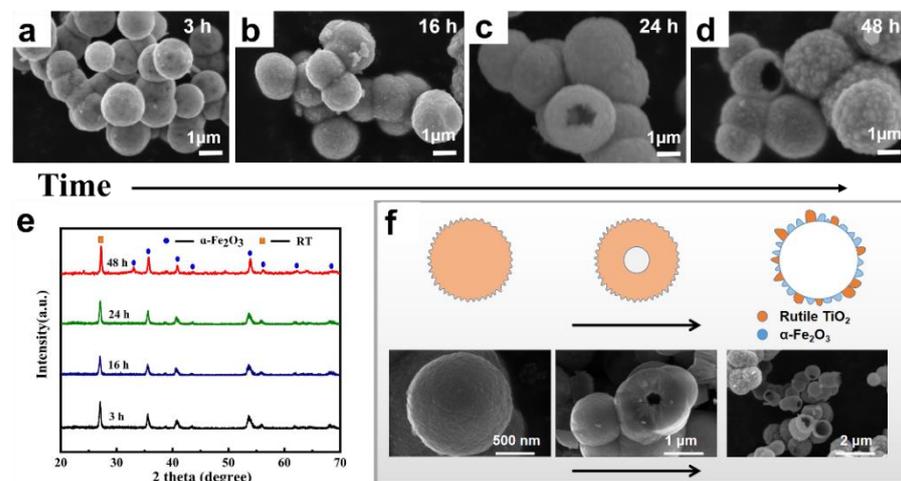

Figure 6. (**a–d**) SEM images of hollow α-Fe_2O_3/RT (0.025 mM), (**e**) XRD patterns of hollow α- Fe_2O_3/RT (0.025 mM), and (**f**) schematic illustration of the formation of hollow α-Fe_2O_3/RT nanospheres.

As shown in Figure 7a, α-Fe_2O_3 and RT showed a type II isotherm, which exhibits a non-porous structure, and the isotherms of α-Fe_2O_3/RT samples were of the type IV hysteresis loop from 0.5 to 1.0 (P/P_0) [15]. The pore distribution of the composite materials was 2–20 nm (Figure 7b), which indicates that the composite materials were mesopore structures [14]. The formation of nanopores may have been due to the accumulation of self-assembled units. The specific surface area of α-Fe_2O_3/RT (0.025 mM), α-Fe_2O_3/RT (0.042 mM), α-Fe_2O_3/RT (0 mM), α-Fe_2O_3, and RT was 56, 48, 32, 28, and 26 m^2/g, respectively.

Figure 7. (**a**) N_2 adsorption/desorption isotherm, (**b**) the corresponding pore size distribution of the α-Fe$_2$O$_3$/RT (0 mM), α-Fe$_2$O$_3$/RT (0.025 mM), α-Fe$_2$O$_3$/RT (0.042 mM), α-Fe$_2$O$_3$, and RT.

2.2. Magnetic Properties

Figure 8a,b show the room temperature magnetic hysteresis loops of synthesized α-Fe$_2$O$_3$, RT, and hollow α-Fe$_2$O$_3$/RT structures in a magnetic field sweeping from -15 to 15k Oe and Table S1 (Supplementary Materials) collects the values of remnant magnetization (Mr) and coercivity (Hc). It was inferred from the hysteresis loop that the composite material was paramagnetic [38,39]. The coercivity of the samples, obtained by adding different amounts of H$_2$PO$_4$ anion, increased with the concentration of H$_2$PO$_4$ anions, as shown in Figure 8a,b. The introduction of H$_2$PO$_4$ anions could increase the coercivity by domain wall pinning and/or spin pinning [40]. It has been reported that when the average particle size is larger than 183 nm, the coercivity of α-Fe$_2$O$_3$ increases with the decrease in particle size [41]. In addition to the two above factors, studies show that the appearance of a hollow void could introduce kinks near zero magnetization in the M-H loop due to two vortex states with opposite directions [42]. Therefore, the hollow structures might also have contributed to the smaller coercivity. From this result, we can infer that the composite material can be recycled with magnets to avoid secondary pollution.
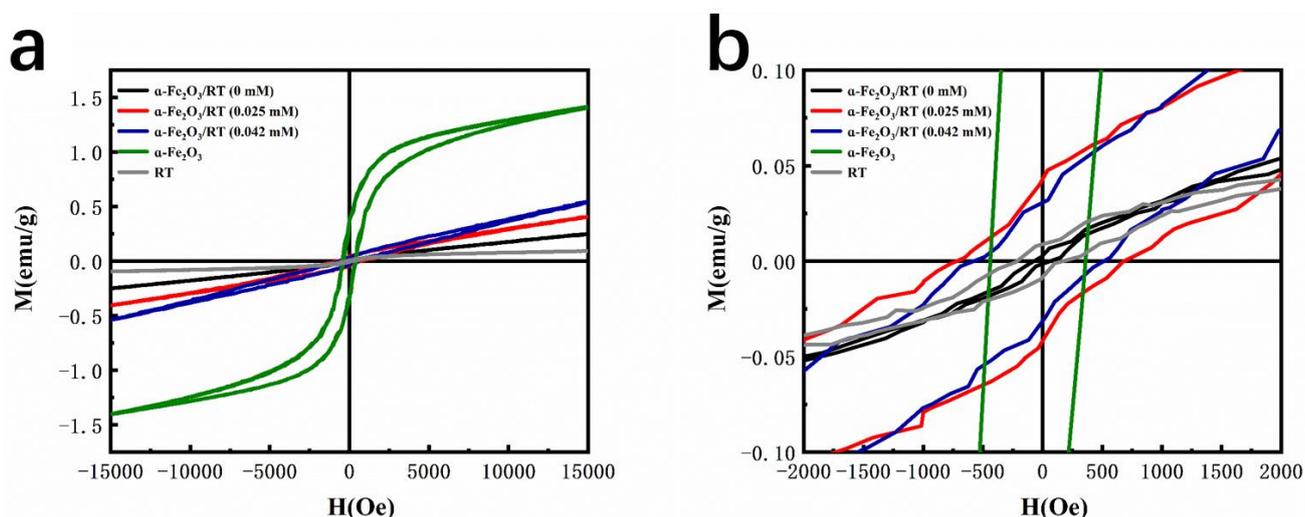

Figure 8. (**a**) Room temperature magnetization loops for the as-obtained samples: α-Fe$_2$O$_3$/RT (0 mM), α-Fe$_2$O$_3$/RT (0.025 mM), α-Fe$_2$O$_3$/RT (0.042 mM), α-Fe$_2$O$_3$, and RT and (**b**) enlarged view of magnetization loops.

2.3. Enhancement of Photocatalytic Activity

The photocatalytic activity of α-Fe$_2$O$_3$/RT is closely related to its energy band. Figure 9a shows the UV-visible absorption spectra of the α-Fe$_2$O$_3$, RT, and α-Fe$_2$O$_3$/RT hollow spheres wavelength of 250–800 nm. α-Fe$_2$O$_3$/RT (0.025 mM) showed stronger absorption from 400 to 800 nm. As shown in Figure 9b–f, α represents the absorption coefficient

(cm^{-1}), hν is the photon energy (eV), A is the equation constant, and Eg is the optical bandgap. The direct optical bandgaps were obtained from the intercept of the linear fitting in the plotted experimental graph of $(\alpha h\nu)^2$ against the photon energy (hν). The optical bandgaps were found to be 2.00, 2.12, 2.08, 2.20, and 3.00 eV for α-Fe$_2$O$_3$/RT (0 mM), α-Fe$_2$O$_3$/RT (0.025 mM), α-Fe$_2$O$_3$/RT (0.042 mM), α-Fe$_2$O$_3$, and RT samples, respectively. This shows that the combined effect of α-Fe$_2$O$_3$ and RT enhanced its absorption capacity and indicates that the composite material formed a heterojunction and changed the bandwidth. The heterojunction structure facilitated the separation of electron and hole pairs, thereby improving photocatalytic performance.
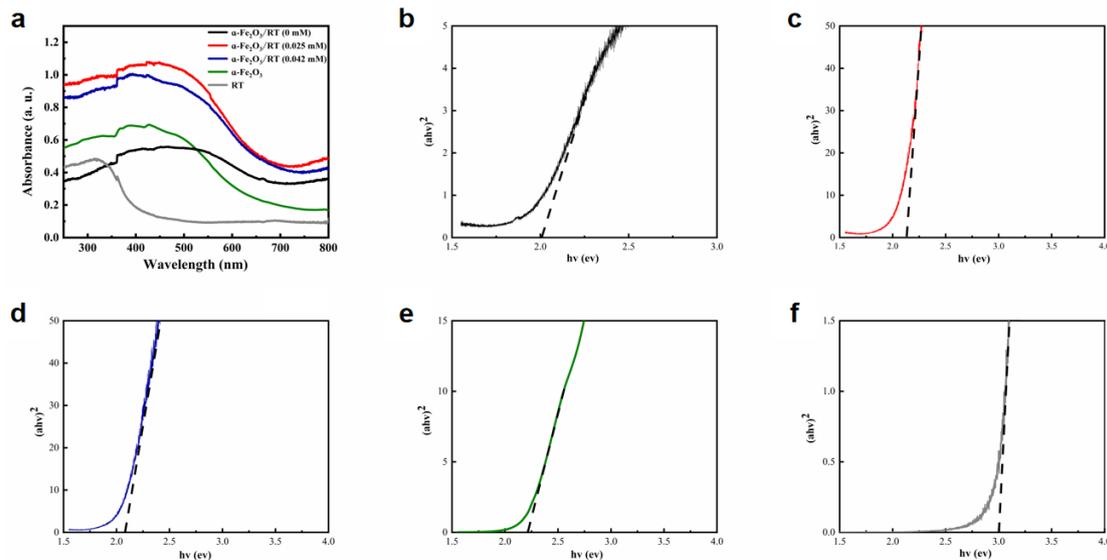

Figure 9. (**a**) UV-vis diffuse reflectance spectra and plots of $(\alpha h\nu)^2$ vs. photon energy hν for samples of (**b**) α-Fe$_2$O$_3$/RT (0 mM), (**c**) α-Fe$_2$O$_3$/RT (0.025 mM), (**d**) α-Fe$_2$O$_3$/RT (0.042 mM), (**e**) α-Fe$_2$O$_3$, and (**f**) RT.

Before the photocatalytic reaction, all samples were subjected to a dark treatment for 30 min for physical adsorption. The catalyst-free pure rhodamine B (RhB) degradation experiment was the reference object. As shown in Figure 10a,b, the absorption peak at 553 nm decreased gradually with increasing irradiation time and almost disappeared after 100 min, indicating that the α-Fe$_2$O$_3$/RT hollow microspheres exhibited excellent photocatalytic activity. In Figure 10c, when the RhB solution was irradiated without a photocatalyst, the degradation rate after 100 min was less than 5%, which was due to the photolysis of the organic dye RhB. For RT, α-Fe$_2$O$_3$, α-Fe$_2$O$_3$/RT (0 mM), α-Fe$_2$O$_3$/RT (0.025 mM), α-Fe$_2$O$_3$/RT (0.042 mM), and α-Fe$_2$O$_3$/RT (0.025 mM) after three months of photocatalysts, the degradation rate of organic dye RhB after 100 min was about 16%, 60%, 76%, 93%, 83%, and 91%, respectively. The α-Fe$_2$O$_3$/RT photocatalyst showed better photocatalytic performance than the α-Fe$_2$O$_3$ and RT photocatalysts, and RT showed extremely little photocatalytic activity under visible light irradiation because it could not be activated by visible light due to its wide energy gap (3.0 eV) [43].
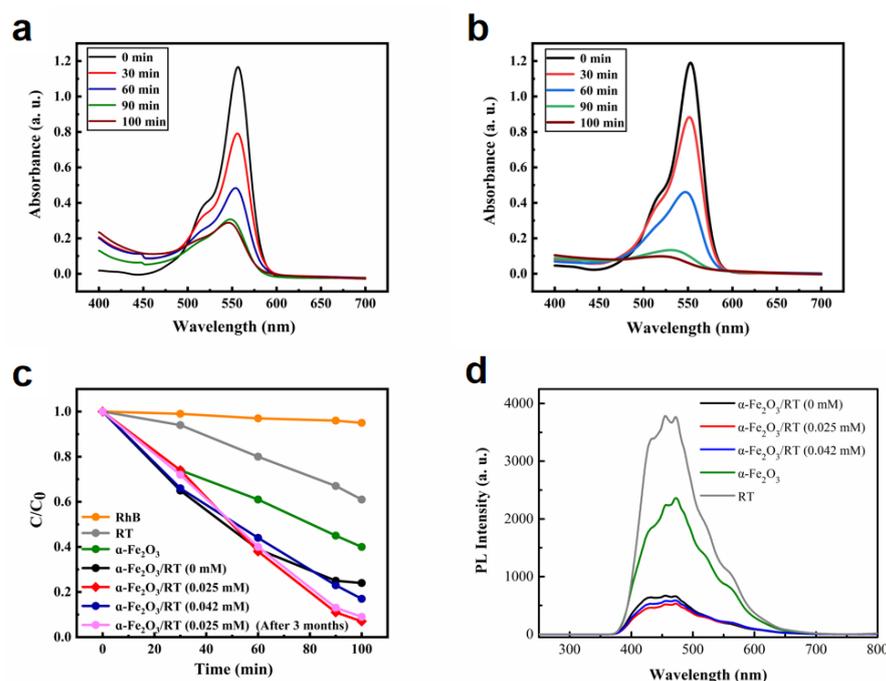
Figure 10. (**a**) Absorption spectra of the RhB solution containing α-Fe$_2$O$_3$/RT (0 mM), (**b**) absorption spectra of the RhB solution containing α-Fe$_2$O$_3$/RT (0.025 mM), and (**c**) photodegradation process of different catalysts towards RhB under visible light irradiation. (**d**) PL spectra for α-Fe$_2$O$_3$, RT, and α-Fe$_2$O$_3$/RT samples (0 mM, 0.025 mM, and 0.042 mM, respectively) measured at 200 nm.

In order to investigate whether charge transfer is possible between α-Fe$_2$O$_3$ and RT, we carried out photoluminescence (PL) measurements, as shown in Figure 10d. Strong emission from pure α-Fe$_2$O$_3$ and RT was observed under 200 nm excitation, but the α-Fe$_2$O$_3$/RT resulted in low emission intensity, and α-Fe$_2$O$_3$/RT (0.025 mM) had the lowest emission intensity. This therefore indicates the efficiency of charge separation and transfer between α-Fe$_2$O$_3$ and RT. The lower recombination rate of electron-hole indeed enhanced the photocatalytic performance. Compared with α-Fe$_2$O$_3$/RT (0 mM) and α-Fe$_2$O$_3$/RT (0.042 mM), α-Fe$_2$O$_3$/RT (0.025 mM) showed better photocatalytic performance. It is likely that the high photocatalytic activity resulted from the hollow structure, large specific surface area, strong absorption of visible light, and low recombination rate of the electron hole [44,45]. α-Fe$_2$O$_3$/RT (0.025 mM) showed a larger specific surface area (56 m^2/g) than α-Fe$_2$O$_3$/RT (0 mM) and α-Fe$_2$O$_3$/RT (0.042 mM). A larger specific surface area provides more active sites for photocatalytic reactions. Therefore, the photo-generated charge carriers could more easily transfer to the surface to degrade the adsorbed organic dyes. In contrast, we also compared the photocatalytic performance with other work. As shown in Table S2, after being compounded with α-Fe$_2$O$_3$, the photodegradation activity of α-Fe$_2$O$_3$/RT improved, which further demonstrates that α-Fe$_2$O$_3$/RT hollow microspheres could be a promising material for degrading organic dyes. An SEM image of the α-Fe$_2$O$_3$/rutile TiO$_2$ (0.025 mM) after placement for three months is shown in Figure S1. The morphology and structure of α-Fe$_2$O$_3$/rutile TiO$_2$ (0.025 mM) showed almost no change, which was very important for maintaining the samples' photocatalytic activity.

Furthermore, the schematic diagrams of the photocatalytic mechanism of α-Fe$_2$O$_3$/RT under UV and visible light irradiation are shown in Figure 11. After contact, the two semiconductors could reach the same Fermi level because of the different work functions of the α-Fe$_2$O$_3$ (5.88 eV) and TiO$_2$ (4.308 eV) [20]; the photoelectrons of α-Fe$_2$O$_3$ could go through the barrier and transfer to the CB (conduction band) of TiO$_2$ due to the CB of TiO$_2$ being lower than that of the α-Fe$_2$O$_3$ [46,47]. These electrons were captured by dissolved oxygen in an aqueous solution to produce the reactive oxygen species ($\cdot$O$_2$). On the contrary, the remaining holes of TiO$_2$ in the VB (valence band) would rapidly

transfer to the VB of α-Fe$_2$O$_3$. H$_2$O traps the holes to form hydroxyl radicals ($\cdot$OH). These reactive oxygen species ($\cdot$O$_2$) and hydroxyl radicals ($\cdot$OH) with high activities can degrade RhB rapidly [48–50]. Therefore, in this wide-narrow band gap composited photocatalysis system, the photogenerated electron-hole pairs are separated at the contact surfaces efficiently and increase the lifetime of the charge carriers [51,52]. The effective separation of the electron-hole pair is the final reason for the improvement of photocatalytic abilities.
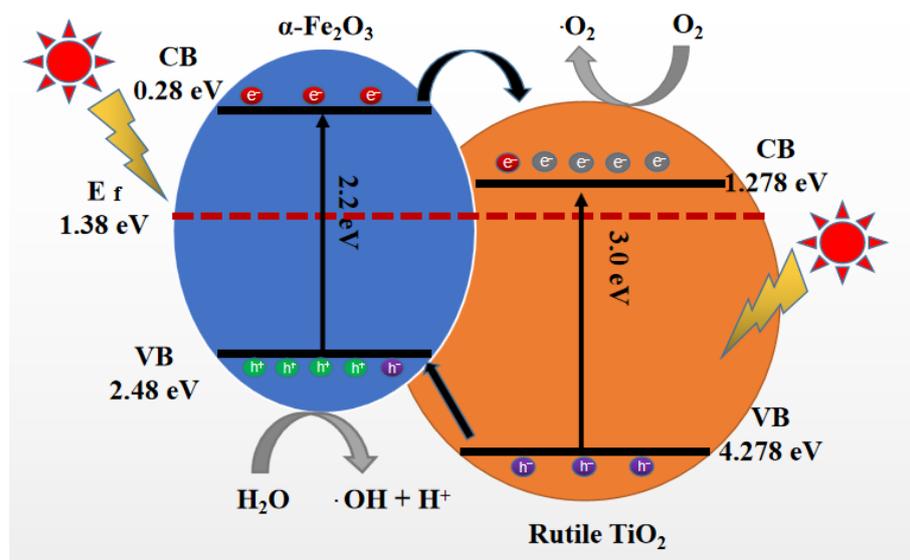

Figure 11. Schematic diagrams of the photocatalytic mechanism of α-Fe$_2$O$_3$/RT.

3. Materials and Methods

3.1. Materials and Techniques

Ferric chloride (FeCl$_3$·6H$_2$O, $\geq$99.0%), sodium dihydrogen phosphate (NaH$_2$PO$_4$, $\geq$99.0%), and sodium fluoride (NaF, $\geq$98.0%) were purchased from Sinopharm Chemical Reagent Co., Ltd. (Ningbo, China). Ammonium fluorotitanate ((NH$_4$)$_2$TiF$_6$, $\geq$98.0%) was purchased from Tianjin Guangfu Fine Chemical Research Institute. Deionized water was used throughout the experiment. Tetrabutyl titanate and ethanol were purchased from Tianjin Yongda Chemical Reagent Co., Ltd, Tianjin, China.

The materials were characterized by X-ray diffraction (XRD) with an MSXD-3 X-ray diffractometer using Cu-Kα radiation (α = 0.15418 nm), and an accelerating voltage of 40 kV and an emission current of 40 mA were employed. Transmission electron microscopy (TEM) observation was carried out on a Tecnai G2 F20 S-TWIN (FEI) instrument operated at 200 kV accelerating voltage. Scanning electron microscopy (SEM) observation was carried out on a Quanta 250 (FEI) operated at an accelerating voltage of 30 kV.

N$_2$ adsorption/desorption isotherms were obtained on a Micromeritics ASAP Tristar II 3020 apparatus. The pore size distribution curves were calculated from the adsorption branch of the N$_2$ isotherm through the Barrett–Joyner–Halenda (BJH) method.

The photocatalyst was exposed to a 300 W xenon lamp (HSX-F/UV 300, Beijing NBeT), using the visible spectrum (390–770 nm) and the intensity was 1900 mW/cm^2.

The photoluminescence measurement was measured by fluorescence spectrometer ((F-4600, Hitachi) at 200 nm.

The magnetic properties of the as-synthesized samples were measured with a physical property measurement system (PPMS-9T, EverCoolII, USA).

3.2. Synthesis of the Rutile TiO$_2$ (RT)

Tetrabutyl titanate was added to the 2 mol/L HCl solution, with the temperature maintained below 10 °C by an ice-water bath. The mixture was heated in a water bath

at 80 °C for 4 h to produce a white suspension. Then the suspension was placed in a hydrothermal reactor and heated at 160 °C for 6 h. It was washed five times with deionized water. After drying at 80 °C in air, RT was obtained.

3.3. Synthesis of the α-Fe₂O₃

$FeCl_3 \cdot 6H_2O$ (0.75 g, 2.7 mM), NaF (0.126 g, 3 mM), and NaH_2PO_4 (0.003 g, 0.025 mM) were added to 60 mL of deionized water. After sonication for 30 min, the solution was transferred to a Polytetrafluoroethylene (PTFE)-lined stainless-steel autoclave with a capacity of 70 mL and kept at 220 °C for 48 h. The sample was washed 5 times with deionized water and ethanol. After drying in a vacuum oven at 80 °C for 10 h, the final samples were obtained.

3.4. Synthesis of Hollow α-Fe₂O₃/RT Nanospheres

$FeCl_3 \cdot 6H_2O$ (0.75 g, 2.7 mM), $(NH_4)_2TiF_6$ (0.55 g, 2.8 mM), NaF (0.126 g, 3 mM), and NaH_2PO4 (0.003 g, 0.025 mM) were added to 60 mL of deionized water. After sonication for 30 min, the solution was transferred to a PTFE-lined stainless-steel autoclave with a capacity of 70 mL and kept at 220 °C for 48 h. The sample was washed 5 times with deionized water and ethanol. After drying in a vacuum oven at 80 °C for 10 h, the final samples were obtained.

3.5. Photocatalytic Reaction

The experimental conditions were as follows: The photocatalytic reaction system consisted of a 300W Xenon lamp equipped with a UV filter and placed above the RhB solution with a distance of about 10 cm, which was mounted with a 400 nm cut-off glass filter. A total of 20.0 mg of α-Fe₂O₃/RT photocatalyst and 50.0 mL of RhB dye aqueous solution (30.0 mg/L) were mixed in a Pyrex reactor and stirred in the dark for 30 min. After that, the mixed solution was exposed to a 300W xenon lamp while stirring. Subsequently, 3.0 mL of the suspension were centrifuged at 10,000 rpm for 15 min to remove the photocatalyst. Finally, by monitoring the absorbance at 553 nm, the concentration of RhB was monitored with a TU-1901 ultraviolet-visible spectrophotometer.

4. Conclusions

A self-assembled paramagnetic α-Fe₂O₃/RT hollow sphere composite structure with controllable morphology was successfully synthesized via a template-free hydrothermal method. The α-Fe₂O₃/RT hollow sphere assembled by nanoparticles and nanocubes had good crystallinity and a large specific surface area. The self-assembled structure provided more exposed active sites and improved the light absorbance. A time-dependent experiment confirmed the hollow structure formed by the Ostwald ripening process. Phosphate played a significant role in forming α-Fe₂O₃/RT hollow spheres, and the hollow structure was beneficial to improving the photocatalytic performance. We believe that the formation of a heterojunction between α-Fe₂O₃ and RT promoted photogenerated electrons and holes, which helped prolong the carrying time and then encourage charge separation. Therefore, the degradation rate of RhB with α-Fe₂O₃/RT (0.025 mM) was up to 93% after 100 min. In addition, the synthesized samples showed paramagnetism and could be easily recycled. After compounding, the α-Fe₂O₃/RT composite material had a visible light response and has potential application prospects in the photocatalytic degradation of organic dyes.

References

1. Asaithambi, S.; Sakthivel, P.; Karuppaiah, M. Influence of Ni Doping in SnO_2 Nanoparticles with Enhanced Visible Light Photocatalytic Activity for Degradation of Methylene Blue Dye. *J. Nanosci. Nanotechnol.* **2019**, *19*, 4438–4446. [CrossRef]
2. Idrus-Saidi, S.; Tang, J.; Ghasemian, M.; Yang, J.; Han, J.-L.; Syed, N.; Daeneke, T.; Abbasi, R.; Koshy, P.; O'Mullane, A.; et al. Liquid metal core-shell structures functionalised via mechanical agitation: The example of Field's metal. *J. Mater. Chem. A* **2019**, *7*, 17876. [CrossRef]
3. Kment, S.; Riboni, F.; Pausova, S.; Wang, L.; Han, H. Photoanodes based on TiO_2 and α-Fe_2O_3 for solar water splitting-the superior role of 1D nanoarchitecture and combined heterostructures. *Chem. Soc. Rev.* **2017**, *46*, 3716–3769. [CrossRef]
4. Ghasemian, M.; Mayyas, M.; Idrus-Saidi, S.; Jamal, M.; Yang, J.; Daeneke, T.; Kalantar-Zadeh, K. Self-Limiting Galvanic Growth of MnO_2 Mnolayers on a Liquid Metal-Appled to Photocatalysis. *Adv. Funct. Mater.* **2019**, *29*, 1901649. [CrossRef]
5. Wang, F.Y.; Yang, Q.D.; Xu, G.; Lei, N.Y.; Ho, J.C. Highly active and enhanced photocatalytic silicon nanowire arrays. *Nanoscale* **2011**, *3*, 3269. [CrossRef]
6. Zhang, Z.Q.; Bai, L.L.; Li, Z.J. Review of strategies for the fabrication of heterojunctional nanocomposites as efficient visible-light catalysts by modulating excited electrons with appropriate thermodynamic energy. *J. Mater. Chem. A* **2019**, *7*, 10879. [CrossRef]
7. Gao, C.M.; Wei, T.; Zhang, Y.Y.; Song, X.H.; Huan, Y.; Liu, H.; Chen, X.D. A Photoresponsive Rutile TiO_2 Heterojunction with Enhanced Electron-Hole Separation for High-Performance Hydrogen Evolution. *Adv. Mater.* **2019**, *31*, 1806596. [CrossRef] [PubMed]
8. Yang, Y.Q.; Liu, G.; Cheng, H.M. Enhanced Photocatalytic H_2 Production in Core-Shell Engineered Rutile TiO_2. *Adv. Mater.* **2016**, *28*, 1600495. [CrossRef] [PubMed]
9. Luan, P.; Xie, M.; Liu, D.N. Effective charge separation in the rutile TiO_2 nanorod-coupled α-Fe_2O_3 with exceptionally high visible activities. *Sci. Rep.* **2014**, *4*, 6180. [CrossRef] [PubMed]
10. Sun, J.; Gao, L.; Zhang, Q. Synthesizing and Comparing the Photocatalytic Properties of High Surface Area Rutile and Anatase Titania Nanoparticles. *J. Am. Ceram. Soc.* **2003**, *86*, 1677–1682. [CrossRef]
11. Ohno, T.; Furukawa, K.; Matsumura, M. Photocatalytic Activities of Pure Rutile Particles Isolated from TiO2 Powder by Dissolving the Anatase Component in HF Solution. *J. Phys. Chem. B* **2001**, *105*, 2417–2420. [CrossRef]
12. Naya, S.; Nikawa, T.; Kimura, K.; Tada, H. Rapid and Complete Removal of Nonylphenol by Gold Nanoparticle/Rutile Titanium (IV) Oxide Plasmon Photocatalyst. *ACS Catal.* **2015**, *3*, 10–13. [CrossRef]
13. Xia, C.X.; Wang, H.; Kim, J.K.; Wang, J.Y. Rational Design of Metal Oxide-Based Heterostructure for Efficient Photocatalytic and Photoelectrochemical Systems. *Adv. Funct. Mater.* **2020**, 2008247. [CrossRef]
14. Xu, H.F.; Li, G.; Zhu, G.; Zhu, K.-R.; Jin, S.-W. Enhanced photocatalytic degradation of rutile/anatase TiO_2 heterojunction nanoflowers. *Catal. Commun.* **2015**, *62*, 52–56. [CrossRef]
15. Ghosh, M.; Liu, J.W.; Steven, S.; Chuang, C.; Jana, S.-C. Fabrication of Hierarchical V_2O_5 Nanorods on TiO_2 Nanofibers and Their Enhanced Photocatalytic Activity under Visible Light. *ChemCatChem* **2018**, *10*, 3305. [CrossRef]
16. Zhang, R.-N.; Sun, M.-L.; Zhao, G.-D.; Yin, G.-C.; Liu, B. Hierarchical Fe_2O_3 nanorods/TiO_2 nanosheets heterostructure: Growth mechanism, enhanced visible-light photocatalytic and photoelectrochemical performances. *Appl. Surf. Sci.* **2019**, *475*, 380–388. [CrossRef]
17. Kevin, S.; Radek, Z.; Florian, L.F.; Rosa, R. Photoelectrochemical Water Splitting with Mesoporous Hematite Prepared by a Solution-Based Colloidal Approach. *J. Am. Chem. Soc.* **2010**, *132*, 7436–7444.
18. Tao, Q.Q.; Huang, X.; Bi, J.T.; Yu, L.; Hao, H.X. Aerobic Oil-Phase Cyclic Magnetic Adsorption to Synthesize 1D Fe_2O_3@TiO_2 Nanotube Composites for Enhanced Visible-Light Photocatalytic Degradation. *Nanomaterials* **2020**, *10*, 1345. [CrossRef] [PubMed]
19. Wang, T.; Yang, G.D.; Liu, J.; Yang, B.L. Orthogonal synthesis, structural characteristics, and enhanced visible-light photocatalysis of mesoporous Fe_2O_3/TiO_2 heterostructured microspheres. *Appl. Surf. Sci.* **2014**, *311*, 314–323. [CrossRef]
20. Liu, J.; Yang, S.L.; Wu, W.; Tian, Q.Y.; Cui, S.Y.; Dai, Z.G.; Ren, F. 3D Flowerlike α-Fe_2O_3@TiO_2 Core-Shell Nanostructures: General Synthesis and Enhanced Photocatalytic Performance. *ACS Sustain. Chem. Eng.* **2015**, *3*, 2975–2984. [CrossRef]

21. Xie, M.Z.; Meng, Q.Q.; Luan, P.; Feng, Y.-J. Synthesis of mesoporous TiO_2-coupled Fe_2O_3 as efficient visible nano-photocatalysts for degrading colorless pollutants. *RSC Adv.* **2014**, *4*, 520–527. [CrossRef]

22. Wang, Z.Y.; Zhou, L.; Lou, X.-W. Metal Oxide Hollow Nanostructures for Lithium on Batteries. *Adv. Mater.* **2012**, *24*, 1903–1911. [CrossRef] [PubMed]

23. Yang, G.D.; Yang, B.L.; Xiao, T.C.; Yan, Z.F. One-step solvothermal synthesis of hierarchically porous nanostructured CdS/TiO_2 heterojunction with higher visible light photocatalytic activity. *Appl. Surf. Sci.* **2013**, *283*, 402–410. [CrossRef]

24. Xiang, L.Q.; Zhao, X.P.; Yin, J.B.; Fan, B.L. Well-organized 3D urchin-like hierarchical TiO_2 microspheres with high photocatalytic activity. *J. Mater. Sci.* **2012**, *47*, 1436–1445. [CrossRef]

25. Gao, P.; Sun, D.D. Ultrasonic Preparation of Hierarchical Graphene-Oxide/TiO_2 Composite Microspheres for Efficient Photocatalytic Hydrogen Production Chem. *Asian J.* **2013**, *8*, 2779–2786. [CrossRef]

26. Xiang, Q.J.; Yu, J.G.; Cheng, B.; Ong, H.C. Microwave-Hydrothermal Preparation and Visible-Light Photoactivity of Plasmonic Photocatalyst Ag-TiO_2 Nanocomposite Hollow Spheres. *Chem. Asian J.* **2010**, *5*, 1466–1474. [CrossRef] [PubMed]

27. Andersson, M.; Kiselev, A.; Osterlund, L. Microemulsion-mediated room-temperature synthesis of high-surface-area rutile and its photocatalytic performance. *J. Phys. Chem. C* **2007**, *111*, 6789–6797. [CrossRef]

28. Murray, J.; Kirwan, L.; Loan, M.; Hodnett, B.-K. In-situ synchrotron diffraction study of the hydrothermal transformation of goethite to hematite in sodium aluminate solutions. *Hydrometallurgy* **2009**, *95*, 239–246. [CrossRef]

29. Wu, Y.; Zhang, W.; Yu, W.; Liu, H.; Chen, R.; Wei, Y. Ferrihydrite preparation and its application for removal of anionic dyes. *Front. Environ. Sci. Eng.* **2015**, *9*, 411–418. [CrossRef]

30. Žic, M.; Ristić, M.; Musić, S. Effect of phosphate on the morphology and size of α-Fe_2O_3 particles crystallized from dense β-FeOOH suspensions. *J. Alloys Compd.* **2008**, *466*, 498–506. [CrossRef]

31. Žic, M.; Ristić, M.; Musić, S. Precipitation of α-Fe_2O_3 from dense β-FeOOH suspensions with added ammonium amidosulfonate. *J. Mol. Struct.* **2009**, *924–926*, 235–242. [CrossRef]

32. Qi, Z.; Liang, H.; Wei, C.; Wang, Z.; Wang, R. X-shaped hollow α-FeOOH penetration twins and their conversion to α-Fe_2O_3 nanocrystals bound byhigh-index facets with enhanced photocatalytic activity. *Chem. Eng. J.* **2015**, *274*, 224–230.

33. Zhu, L.P.; Wang, L.L.; Bing, N.C.; Huang, C.; Wang, L.J.; Liao, G.H. Porous flfluorine-doped γ-Fe_2O_3 hollow spheres: Synthesis, growth mechanism, and their application in photocatalysis. *ACS Appl. Mater. Interfaces* **2013**, *5*, 12478–12487. [CrossRef]

34. Lou, X.W.; Wang, Y.; Yuan, C.; Lee, J.Y.; Archer, L.A. Template-free synthesis of SnO_2 hollow nanostructures with high lithium storage capacity. *Adv. Mater.* **2006**, *18*, 2325–2329. [CrossRef]

35. Zhu, L.P.; Xiao, H.M.; Zhang, W.-D.; Yang, G.; Fu, S.-Y. One-pot template-free synthesis of monodisperse and single-crystal magnetite hollow spheres by a simple solvothermal route. *Cryst. Growth Des.* **2008**, *8*, 957–963. [CrossRef]

36. Yu, J.; Yu, X.; Huang, B.; Zhang, X.; Dai, Y. Hydrothermal synthesis and visible-light photocatalytic activity of novel cage-like ferric oxide hollow spheres. *Cryst. Growth Des.* **2009**, *9*, 1474–1480. [CrossRef]

37. Niu, K.Y.; Park, J.; Zheng, H.M.; Alivisatos, A.P. Revealing Bismuth Oxide Hollow Nanoparticle Formation by the Kirkendall Effffect. *Nano Lett.* **2013**, *13*, 5715–5719. [CrossRef]

38. Liang, H.; Chen, W.; Jiang, X.; Xu, X.; Xu, B.; Wang, Z. Synthesis of 2D hollow hematite microplatelets with tuneable porosity and their comparative photocatalytic activities. *J. Mater. Chem. A* **2014**, *2*, 4340–4346. [CrossRef]

39. Yin, H.; Zhao, Y.L.; Hua, Q.S.; Zhang, J.M.; Zhang, Y.S.; Yuan, J.S. Controlled Synthesis of Hollow α-Fe_2O_3 Microspheres Assembled With Ionic Liquid for Enhanced Visible-Light Photocatalytic Activity. *Front. Chem.* **2019**, *10*, 3389. [CrossRef] [PubMed]

40. Lv, B.L.; Xu, Y.; Gao, Q.; Wu, D.; Sun, Y.-H. Controllable synthesis and magnetism of iron oxides nanorings. *J. Nanosci. Nanotechnol.* **2010**, *10*, 2348–2359. [CrossRef] [PubMed]

41. Lv, B.L.; Liu, Z.Y.; Tian, H.; Xu, Y.; Wu, D.; Sun, Y.H. Single-Crystalline Dodecahedral and Octodecahedral α-Fe_2O_3 Particles Synthesized by a Fluoride Anion-Assisted Hydrothermal Method. *Adv. Funct. Mater.* **2010**, *20*, 3987–3996. [CrossRef]

42. Li, Z.; Cai, W.; Duan, G.; Liu, P. Magnetic step regions in α-Fe_2O_3 nanostructured ring arrays. *Phys. E* **2008**, *40*, 680–683. [CrossRef]

43. Fang, J.; Shi, F.; Bu, J.; Ding, J.; Xu, S.; Bao, J. One-Step Synthesis of Bifunctional TiO_2 Catalysts and Their Photocatalytic Activity. *J. Phys. Chem. C* **2010**, *114*, 7940–7948. [CrossRef]

44. Wu, W.; Xiao, X.; Zhang, S.; Ren, F.; Jiang, C. Facile Method to Synthesize Magnetic Iron Oxides/TiO_2 Hybrid Nanoparticles and Their Photodegradation Application of Methylene Blue. *Nanoscale Res. Lett.* **2011**, *6*, 533. [CrossRef]

45. Palanisamy, B.; Babu, C.; Sundaravel, B.; Anandan, S.; Murugesan, V. Sol-Gel Synthesis of Mesoporous Mixed Fe_2O_3/TiO_2 Photocatalyst: Application for Degradation of 4-chlorophenol. *J. Hazard. Mater.* **2013**, *252–253*, 233–242. [CrossRef]

46. Peng, L.; Xie, T.; Lu, Y.; Fan, H.; Wang, D. Synthesis, Photoelectric Properties and Photocatalytic Activity of the Fe_2O_3/TiO_2 Heterogeneous Photocatalysts. *Phys. Chem. Chem. Phys.* **2010**, *12*, 8033–8041. [CrossRef] [PubMed]

47. Niu, M.; Huang, F.; Cui, L.; Huang, P.; Yu, Y.; Wang, Y. Hydrothermal Synthesis, Structural Characteristics, and Enhanced Photocatalysis of SnO_2/α-Fe_2O_3 Semiconductor Nanoheterostructures. *ACS Nano* **2010**, *4*, 681–688. [CrossRef] [PubMed]

48. Sridharan, K.; Jang, E.; Park, T.J. Novel visible light active graphitic C_3N_4-TiO_2 composite photocatalyst: Synergistic synthesis, growth and photocatalytic treatment of hazardous pollutants. *Appl. Catal. B* **2013**, *142*, 718–728. [CrossRef]

49. Mrowetz, M.; Balcerski, W.; Colussi, A.J.; Hoffmann, M.R. Oxidative Power of Nitrogen-Doped TiO_2 Photocatalysts under Visible Illumination. *J. Phys. Chem. B* **2004**, *108*, 17269–17273. [CrossRef]

50. Xue, C.; Wang, T.; Yang, G.; Yang, B.; Ding, S. A facile strategy for the synthesis of hierarchical TiO$_2$/CdS hollow sphere heterostructures with excellent visible light activity. *J. Mater. Chem. A* **2014**, *2*, 7674–7679. [CrossRef]
51. Qu, Y.; Duan, X. Progress, challenge and perspective of heterogeneous photocatalysts. *Chem. Soc. Rev.* **2013**, *14*, 2568–2580. [CrossRef] [PubMed]
52. Ji, T.; Ha, E.; Wu, M.Z.; Hu, X.; Wang, J.; Sun, Y.G.; Li, S.J.; Hu, J.Q. Controllable Hydrothermal Synthesis and Photocatalytic Performance of Bi$_2$MoO$_6$ Nano/Microstructures. *Catalysts* **2020**, *10*, 1161. [CrossRef]